ACS APPLIED MATERIALS & INTERFACES

www.acsami.org

Research Article

Stretchable and Recyclable Liquid Metal Droplets Embedded Elastomer Composite with High Mechanically Sensitive Conductivity

Xiaokang He, Jianpeng Wu, Shouhu Xuan,* Shuaishuai Sun, and Xinglong Gong*

Cite This: *ACS Appl. Mater. Interfaces* 2022, 14, 9597−9607

Read Online

ACCESS | Metrics & More | Article Recommendations | Supporting Information

ABSTRACT: Liquid metal (LM)-based elastomers have received growing interest for a wide range of applications such as soft robotics and flexible electronics. This work reports a stretchable and bendable liquid metal droplets embedded elastomer (LMDE) composite, which consists of liquid metal droplets (LMDs) filler and carbonyl iron particles (CIPs)/polydimethylsiloxane (PDMS) hybrid matrix. The reversible switching of the composite from an insulator to a conductor can be realized through the contact and noncontact process between the LMDs. The mechanism of constructing the controllable conductive path between the droplets under external deformations has been systematically studied, and this result also provides a basis model for analyzing the conductive networks in traditional LM-based flexible composites. The composites exhibit stable mechanical and electrical performance under different tensile strains and bending angles. Moreover, the fluidic nature of LM endows the composite with good electrically healing capability. The valuable LM can be easily recycled at a high recovery rate of 98%. Finally, the composite can be developed as a sensor for the detection of both compressive force and magnetic field, demonstrating a broad promising in flexible electronics, actuators, and wearable devices.

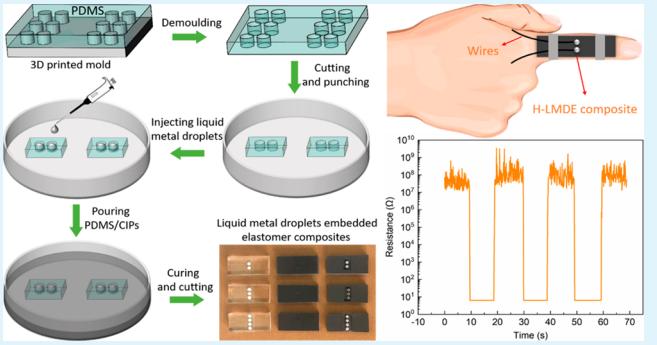

KEYWORDS: *liquid metal droplets, elastomer composites, mechanically sensitive conductivity, mechanic-magnetic detection, recyclability*

1. INTRODUCTION

In the past decade, the flexible and stretchable electronics have attracted significant attention due to the increasing requirements of wearable devices, electronic skins, stretchable displays, flexible sensors, and intelligent robotics.[1−5] The soft and conductive composites are usually fabricated and employed in practical applications due to their good electrical conductivity and deformability. Usually, conductive fillers such as carbon nanotubes,[6] graphene,[7] and metallic microparticles[8,9] are dispersed into the elastomer matrix to achieve the highly conductive, stretchable and flexible features. In addition, the soft composites can also be prepared by forming conductive laminated structures containing the conductive layer and stretchable matrix, such as forming different shapes of metal patterns on a prestretched matrix,[10] conductive network polymer film,[11−13] and the integration of rigid electronic components and soft matrix.[14,15] However, the rigid conductive layer is easily damaged under complex external loadings, resulting in the decrease of conductivity and weakness of the stretchability and flexibility of the composites.

Recently, the liquid phase conductive fillers such as ionic liquid and liquid metal are perfect candidates for fabricating all-soft composites with good shape reconfigurability, stable conductivity and healing capability. Particularly, Gallium-based liquid metal alloys, such as eutectic gallium indium (EGaIn) and eutectic gallium indium tin (GaInSn), are in the atypical liquid state at room temperature while featuring high thermal/electrical conductivity, negligible toxicity, superb fluidity, and large deformability in their liquid state.[16−19] In comparison to the ionic liquid, the oxide layer formed on the surface of liquid metal helps to maintain its shape, which endows it with the possibility of recycling from the composites. The liquid metals are usually printed or encapsulated in elastomer substrate and then sealed with an elastomer cover.[20−22] Such fabrication process produced ideal flexible and stretchable composites, which could respond to the external stimuli like stretching, bending, and twisting. However, the liquid metal has the risk of leaking from the matrix under complex external deformation conditions, which will reduce the mechanical properties and structural stability of the composites. To our knowledge, the direct mixing of LM with elastomer matrix is gradually used to prepare LM-based flexible composites with satisfactory properties.

Received: December 7, 2021
Accepted: January 26, 2022
Published: February 9, 2022

https://doi.org/10.1021/acsami.1c23658
ACS Appl. Mater. Interfaces 2022, 14, 9597−9607

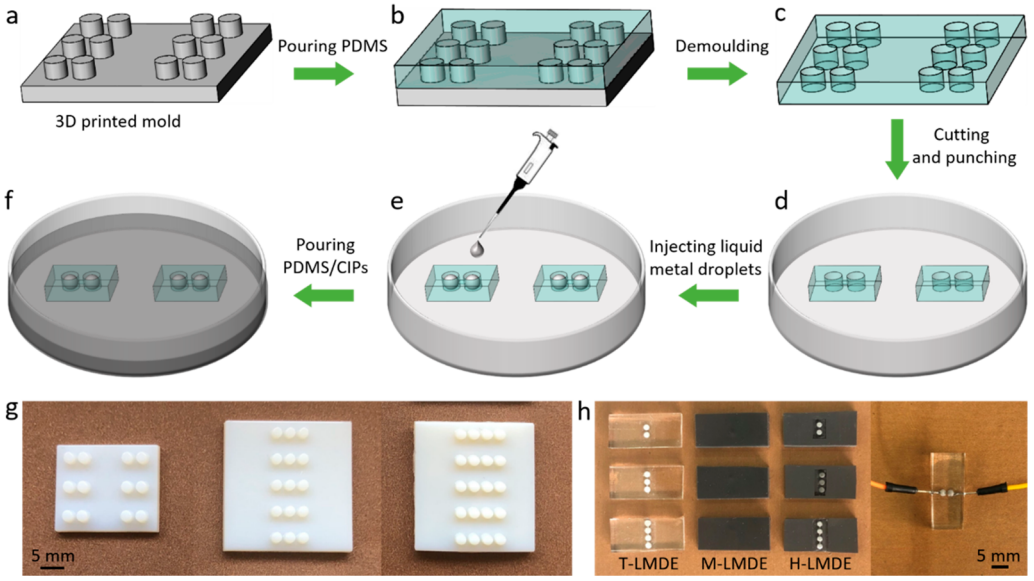

Figure 1. (a–f) Schematic diagram represented the preparation process of H-LMDE composites. (g) Digital images of different kinds of 3D printed molds. (h) Digital images of T-LMDE, M-LMDE, and H-LMDE composites with different numbers of droplets.

To date, versatile LM-based flexible composites, most of which consist of liquid metal droplets (LMDs) and elastomer matrix, have been intensively developed for transient devices,[23,24] actuators and soft robotics,[25,26] high thermal conductive materials,[27,28] and stretchable electrical conductive materials.[29−31] The LMDs with different sizes and morphologies are usually randomly distributed in the matrix of these composites, which also possessed some unique properties including self-healing, recyclability, and good electrical conductivity.[32,33] The LMDs will form a conductive path in the matrix and remain interconnected under external loadings or magnetic fields, but the various sizes and disorderly arrangement of the droplets makes the conductive path vulnerable to external loadings. Besides, high LM contents are commonly required to form a conductive path and achieve a satisfactory electrical conductivity, which brings a series of issues including high cost and metal leakage.[34] Most importantly, the formation mechanism of the conductive paths through the contact between droplets needs to be further studied. Furthermore, the recovery of the valuable LM in the LM-based flexible composites is a challenge due to the strongly bonded networks and the small size of LMDs.[35−37] Therefore, developing a simple strategy capable of fabricating LM-based flexible composites with good mechanical properties, satisfactory conductivity and high recyclability is of significance for expanding the application field of LM-based materials and reducing environmental pollution.

In this paper, a kind of liquid metal droplets embedded elastomer (LMDE) composites was developed. The mechanical and magnetic properties of the LMDE composites were systematically investigated. The conductivity of the LMDE composites could be reversibly switched through the contact and noncontact process between the droplets, which helped to provide a basis model for the construction of conductive networks in LM-based flexible composites. In addition, the composites also possessed good thermal conductivity and electrical healability due to the heat transfer and flow characteristics of liquid metal. The embedding droplets in the elastomer matrix significantly improved the recovery rate of liquid metal and reduced the impact of waste materials on the environment.[38] Finally, the LMDE composites also could be used as a sensor to detect the magnetic field, pressure, and the movement of finger joints. The good sensing performance further demonstrated their feasibility toward the future sensing devices.

2. MATERIALS AND METHODS

2.1. Materials and Chemicals. The EGaIn liquid metal (75% gallium, 25% indium, melting point: 16 °C, density: 6.25 g/cm^3) was purchased from Yongcheng Co., Ltd., China. The carbonyl iron particles (CIPs, type CN, BASF), with an average size of 6 μm, were purchased from Sigma-Aldrich. The polydimethylsiloxane (PDMS) precursor and curing agent (Sylgard 184) were all purchased from Dow Corning. Hydrochloric acid (HCl) was obtained from Sinopharm Chemical Reagent Co., Ltd. NdFeB magnets were purchased from Chizan Co., Ltd., China.

2.2. Preparation of the LMDE Composites. First, the PDMS precursor and curing agent were mixed in a weight ratio of 25:1. The mixture was carefully poured into a 3D-printed mold and treated by vacuum oven for 10 min to remove the bubbles before experiencing a solidification at 80 °C for 1 h. After demolding and cutting, PDMS film with cylindrical array grooves (2 mm in diameter and 1.5 mm in depth) was obtained and a hole puncher with a diameter of 300 μm was used to produce through holes between the grooves. Then the liquid metal droplets (LMDs) treated with HCl solution were injected into the cylindrical array grooves by a pipet. Afterward, the PDMS films embedded with LMDs were sealed by the mixture of PDMS precursor and curing agent (weight ratio 25:1). Finally, a transparent non-magnetic LMDE (T-LMDE) composites was fabricated after curing and cutting. The carbonyl iron particles (CIPs) were mixed with PDMS precursor and curing agent to prepare magnetic LMDE (M-LMDE) composites. Furthermore, the hybrid LMDE (H-LMDE) composites were prepared by using CIPs doped PDMS to encapsulate the transparent PDMS films containing LMDs. Compared with T-LMDE and M-LMDE composites, the H-LMDE composites had both transparency, magnetism and similar mechanical properties. Therefore, the H-LMDE composites were selected as the research object of this paper.

2.3. Characterization. The morphology of H-LMDE composites was characterized by scanning electron microscopy (SEM) and related energy-dispersive X-ray spectrum (EDX) (SEM 500, Zeiss, Ltd.). The digital and thermal images were captured using a digital camera (D1700, Nikon) and thermal camera (ImageIR 8300, InfraTec

https://doi.org/10.1021/acsami.1c23658
ACS Appl. Mater. Interfaces 2022, 14, 9597−9607

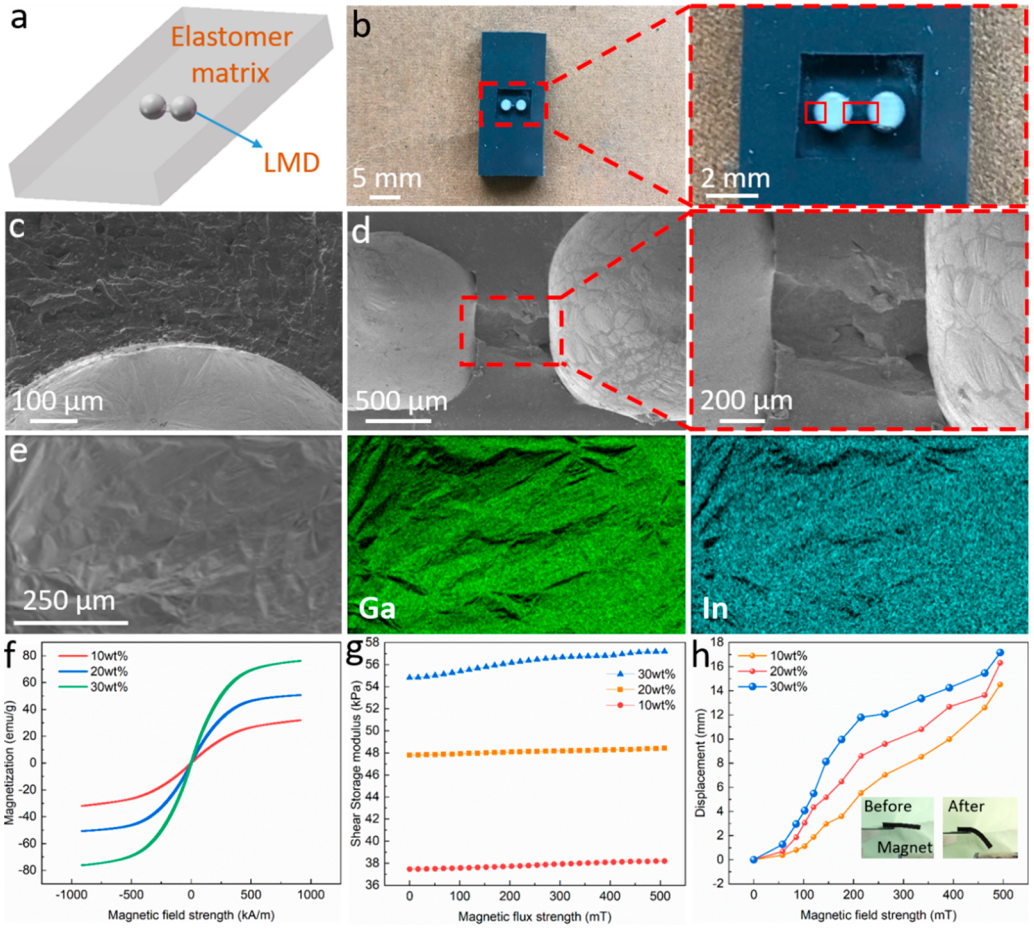

Figure 2. (a,b) The schematic and digital images of the H-LMDE composites. (c) The SEM image of interface between the LMDs and the elastomer matrix. (d) The cross-sectional SEM image of the microchannel between the LMDs in the composites. (e) EDS mapping of the surface for the LMDs. (f,g) Magnetization curves and storage modulus of the elastomer matrix with CIP content of 10, 20, and 30 wt %. (h) The deformation of H-LMDE composites under different magnetic field strengths.

Germany). Hysteresis Measurement of Soft and Hard Magnetic Materials (HyMDC Metis, Leuven, Belgium), and a commercial rheometer (Physica, MCR 302, Anton Paar Co., Austria) were used to test the magnetic and rheological properties of the H-LMDE composites. A dynamic mechanical analyzer (DMA, ElectroForce 3200, TA Instruments, Minnesota 55344, U.S.) was utilized to test the mechanical properties of the H-LMDE composites. The Modulab material test system (Solartron analytical, AMETEK advanced measurement technology, Inc., United Kingdom) was used to evaluate the electrical performance. The thermal conductivities of the samples were measured by a Hot Disk TPS 2500S. A N52 typed magnet was employed to generate magnetic field, and the magnetic flux density was measured by a Tesla meter (HT20, Shanghai Hengtong magnetic technology Co. Ltd., China).

3. RESULTS AND DISCUSSION

3.1. Preparation of the H-LMDE Composites. 3D-printed molds were employed to assist the fabrication of H-LMDE composites (Figure 1a–f). The PDMS precursor and curing agent (weight ratio 25:1) were drop-cast onto a 3D-printed mold with cylindrical protrusions. After curing and demolding, a PDMS film with many cylindrical grooves was obtained. Then, the PDMS film was divided and a microhole with a diameter of about 300 μm was punched between the grooves. Liquid metal droplets (LMDs) were injected in the cylindrical grooves and the CIPs doped PDMS precursor and curing agent were used to seal the PDMS film. After curing for 60 min under 80 °C, the H-LMDE composite with both magnetism and transparency was obtained. The droplets were arranged horizontally in the composites, which was more convenient to the formation of conductive paths than the vertical arrangement of the droplets (Supporting Information (SI) Figure S1). The weight fractions of CIPs were set as 10, 20, and 30 wt % to explore the effect of magnetic particles on the properties of the composites. Using different forms of 3D printing molds, the number and shape of LMDs embedded in the composites could be controlled (Figure 1g and SI Figure S2). The T-LMDE, M-LMDE, and H-LMDE composites with different numbers of LMDs were shown in Figure 1h. Due to the opacity of the matrix, the distribution of LMDs cannot be observed in the M-LMDE composites. However, it could be clearly seen that the droplets were uniformly distributed and neatly arranged in the T-LMDE and H-LMDE composites. Copper wires were buried on both sides of the composites to serve as electrodes.

The H-LMDE composite was composed of LMDs embedded transparent PDMS array and magnetic elastomer matrix, and there was a microchannel between the two droplets (Figure 2a). Figure 2b illustrates the top view of the H-LMDE composite embedded with two LMDs and an enlarged view of the middle part. The droplets were well sealed in the elastomer matrix without leakage, and the deformation of the droplets could be clearly observed due to the transparency of the PDMS array. Figure 2c shows the scanning electron microscope (SEM) image

https://doi.org/10.1021/acsami.1c23658
ACS Appl. Mater. Interfaces 2022, 14, 9597−9607

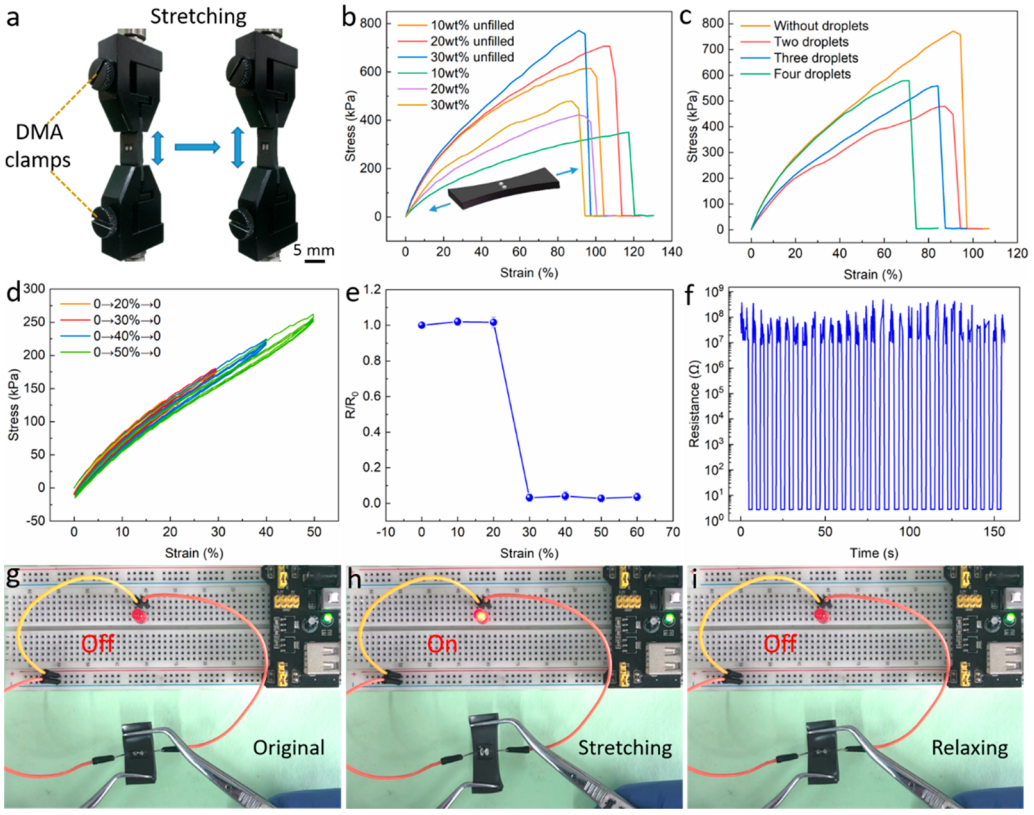

Figure 3. (a) Digital images of the tensile test system, scale bar: 5 mm. (b) Stress versus strain curves of two LMDs embedded H-LMDE composites and unfilled composites as a function of the CIP content. (c) Stress versus strain curves of the unfilled and H-LMDE composites embedded with different numbers of droplets (30 wt % CIP content). (d) Stress−strain curves of two LMDs embedded H-LMDE composite with 30 wt % CIP content for cyclic tensile loading. (e) The normalized resistance of the two LMDs embedded H-LMDE composite (30 wt % CIP content) during the stretching process. (f) The corresponding resistance variation of the two LMDs embedded H-LMDE composite during cyclic stretching at 30% strain. (g−i) Digital images of using the two LMDs embedded H-LMDE composite to realize the switch of a LED.

of interface between the LMDs and the elastomer matrix, where the liquid metal was silver-gray and the elastomer matrix was black. The cross-sectional SEM image of the H-LMDE composite embedded with two LMDs is shown in Figure 2d. The LMDs were fully filled in the cylindrical grooves due to their high surface tension,[39] and the magnified cross-sectional SEM image indicated that there was a microchannel between the two droplets. The wrinkles on the surface of the droplets were caused by the oxidation of the liquid metal when exposed to the air. In order to prevent oxidation of the liquid metal surface from reducing its fluidity, the cylindrical grooves and the intermediate microchannel were treated with dilute hydrochloric acid (HCl) solution before filling the droplets. The energy dispersive X-ray spectrometer (EDS) mapping showed there were Ga and In elements in the liquid metal (Figure 2e). As observed in the EDS mapping of the elastomer matrix, there were Fe and Si elements and the Fe particles were well distributed throughout the matrix with minimal aggregation (SI Figure S3).

The elastomer matrix of the H-LMDE composites with different CIP contents were tested by HyMDC to evaluate the magnetic properties. All the elastomer matrix exhibited soft magnetic behavior and its hysteresis loop was smooth and no hysteresis was found (Figure 2f). The saturation magnetization was 31.9 emu/g, 50.6 emu/g and 76.1 emu/g for the elastomer matrix with CIP content of 10, 20, and 30 wt %, respectively. The variation tendency of saturation magnetization was coincident with CIP content of the elastomer matrix, which reflected the stable magnetization performance of CIPs inside the composites substrate. The shear storage modulus of the matrix evidently increased with the magnetic field under the shear frequency of 5 Hz and strain amplitude of 0.1% (Figure 2g). In order to measure the deformation ability of the composites under the magnetic field, the composite was fixed vertically above a N52 typed magnet. The magnetic field strength generated by the N52 typed magnet could reach up to about 500 mT (SI Figure S4). The displacement was recorded when the magnet gradually approached the composite. The composite with higher CIP content had larger displacement under the same magnetic field. The deformation of the composite increased with the decrease of the distance between the composite and the magnet (Figure 2h), which indicated that the composite had a good deformability under the magnetic field.

3.2. Mechanical and Electrical Properties of the H-LMDE Composites. The mechanical performance of H-LMDE composites was first investigated. During the test, the H-LMDE composite was fixed with the clamps of DMA and tested under tensile strain with cyclic sine waveform (Figure 3a). Representative stress−strain curves for the two LMDs embedded H-LMDE composites with CIP content of 10, 20, and 30 wt % are presented in Figure 3b. With the increase of CIP content, the tensile strength of H-LMDE composites and unfilled composites both gradually increased. The tensile strength of the H-LMDE composite reached to 478 kPa when the CIP content increased to 30 wt %, which attributed to the improvement in the elastic modulus of the elastomer matrix (SI Figure S5). Although embedded with LMDs, the elongation at

https://doi.org/10.1021/acsami.1c23658
ACS Appl. Mater. Interfaces 2022, 14, 9597−9607

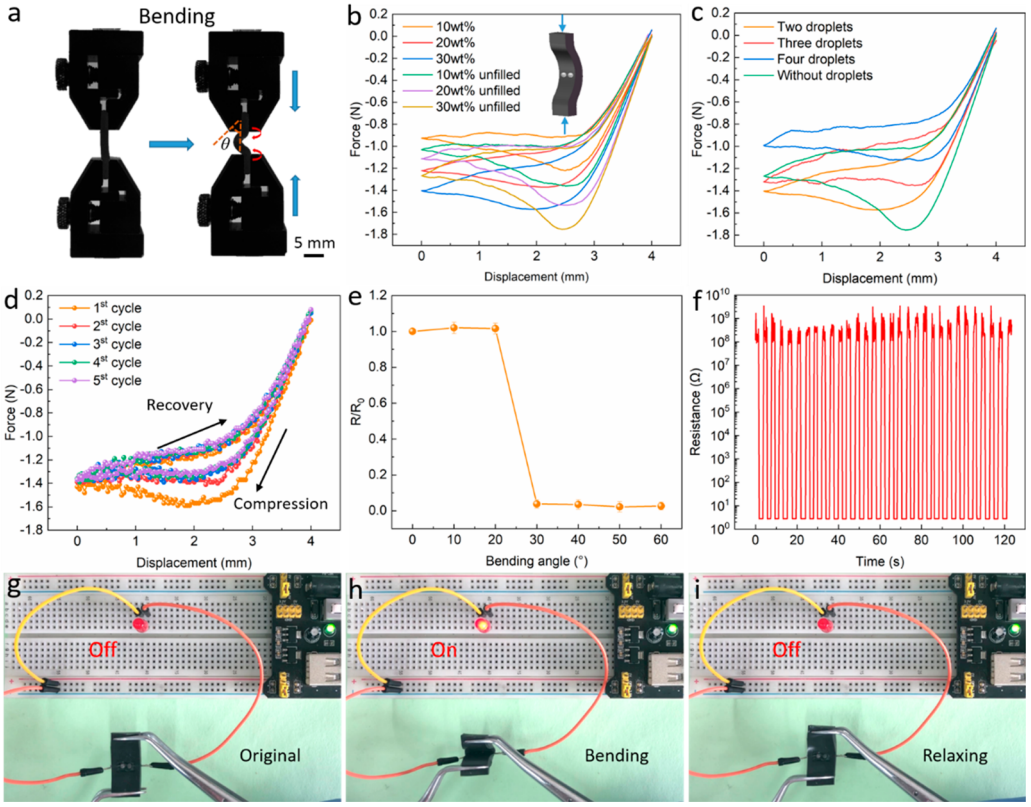

Figure 4. (a) Digital images of the bending test system, scale bar: 5 mm. (b) Force versus displacement curves of two LMDs embedded H-LMDE composites and unfilled composites as a function of the CIP content. (c) Force versus displacement curves of the unfilled and H-LMDE composites embedded with different numbers of droplets (30 wt % CIP content). (d) Force versus displacement curves of the two LMDs embedded H-LMDE composite with 30 wt % CIP content under cyclic bending. (e) The normalized resistance of the two LMDs embedded H-LMDE composite (30 wt % CIP content) during the bending process. (f) The corresponding resistance variation of the two LMDs embedded H-LMDE composite during cyclic bending under the bending angle of 60°. (g–i) Digital images of using the two LMDs embedded H-LMDE composite to realize the switch of LED.

break of H-LMDE composites could still reach a value of up to 120% tensile strain. For the H-LMDE composites with a CIP content of 30 wt %, the tensile strength gradually improved as the number of droplets increased (Figure 3c). This phenomenon was ascribed to that the LMDs increased the surface tension of the solid–liquid interface and improved the adhesion between the droplets and the matrix.[40] As illustrated in Figure 3d, successive loading–unloading tests at increasing tensile strains from 20% to 50% were conducted to evaluate the mechanical hysteresis of the two LMDs embedded H-LMDE composites with 30 wt % CIP content. The stress–strain hysteresis curve of two consecutive cycles overlapped after repeated tests, which can be ascribed to the Mullin's effect.[41] These results demonstrated that the as-fabricated H-LMDE composites were mechanically robust and highly stretchable.

Next, the electrical properties of the H-LMDE composites upon stretching were studied to evaluate the conductivity of the composites. Notably, the composites were electrically insulating when initially prepared because no conductive path was formed in the elastomer matrix. Copper wires were inserted on both sides of the composite along the arrangement direction of the droplets to deliver the electrical signals to Modulab system. The resistance variation was defined as $\Delta R = R/R_0$, R_0 was the initial resistance. The ΔR decreased from 1 to around 0 when the tensile strain of the composite exceeded 20%, which indicated that the composite changed from insulating to conductive (Figure 3e). As the tensile strain increased, the value of ΔR was stable because the conductive path still remained interconnected under external deformations. Then, the resistance change of the composite under cyclic stretching with a tensile strain of 30% was studied at the tensile frequency of 0.2 Hz. As shown in Figure 3f, the composite exhibited a periodic change from conductor to insulator in each stretch-release cycle. For the three and four LMDs embedded H-LMDE composites, they also had the similar electrical properties (SI Figure S6). This benefited from the contact and noncontact process of the LMDs inside the composite, which indicated a good capability of constructing controllable conductive path. The composite was further applied in a circuit switch to realize the on–off control of a light emitting diode (LED) through stretching and releasing process (Figure 3g-i). The LED turned on because the resistance of the circuit decreased when stretching the composite and it turned off after the tension was released (SI Movie S1).

Moreover, the mechanical and electrical properties of the two LMDs embedded H-LMDE composites during the bending process were also explored. Here, the bending angle θ at the two sides was defined as the rotation of upper and lower part from the central axis (Figure 4a). The bending angle θ increased with the compressive displacement. Representative force–displacement curves of the two LMDs embedded H-LMDE composites with different CIP contents are presented in Figure 4b. The bending force was negative since the compression displacement was along the negative direction of the Y axis. Similarly, due to the modulus variation of the elastomer matrix, the bending stiffness of the unfilled composites and H-LMDE composites both increased with the CIP content. The maximum bending

https://doi.org/10.1021/acsami.1c23658
ACS Appl. Mater. Interfaces 2022, 14, 9597–9607

force of the H-LMDE composite during the bending process was 1.61 N when the compression displacement reached 2 mm. As the number of droplets increased, the bending stiffness of the H-LMDE composites with 30 wt % CIP content decreased slightly (Figure 4c). However, the H-LMDE composites still had good bending properties due to the soft nature of liquid metal and high flexibility of PDMS matrix. After keeping the test frequency at 0.01 Hz, the two LMDs embedded H-LMDE composites with 30 wt % CIP content feasibly deformed and quickly recovered during each bend-release cycle, where hysteresis loops suggested a viscoelastic mechanical property for the composites (Figure 4d).

Afterward, we further evaluated the electrical responses of the two LMDs embedded H-LMDE composites at various bending angles (Figure 4e). The ΔR decreased from 1 to around 0 when θ exceeded 20° and the variation tendency indicated that the composite could also change from electrically insulating to conductive in the bending progress. As θ increased, the deformation of the composite became larger and the conductive path could maintain interconnected during this process. Similar to the cyclic tensile tests, when the bending angle changed repeatedly from 0 to 60° at the bending frequency of 0.25 Hz, the resistance R also changed periodically (Figure 4f). This was due to the repeated contact and noncontact process of the internal droplets at the middle microchannel when the composite was squeezed. This feature enabled the composite to realize the on−off control of a LED circuit by bending. The switching process of the LED was successfully realized through the bending and release of the composite (Figure 4g−i). Similar to the stretching process, the LED turned on when the composite was bent and turned off after it was released. Besides the stretching and bending process, the H-LMDE composites also possessed the similar electrical properties under cyclical compression and magnetic field (SI Figure S7). These results demonstrated that the as-fabricated H-LMDE composites possessed stable mechanical properties and good conductive controllability.

In order to explore the construction mechanism of the controllable conductive paths inside the H-LMDE composites, the contact and noncontact process of LMDs in the microchannel was analyzed by both experiments and numerical simulation. The contact and noncontact process were mainly actuated by the elastomer matrix's deformation and capillary breakup effect. Initially, the LMDs were separated from each other in the composite without external forces. As the strain of the composites increased, the LMDs deformed and gradually contacted with each other in the microchannel, forming a liquid metal (LM) bridge (Figure 5a). At the same time, the dynamic change process of the LM bridge was also captured by a high-speed video camera (Nikon, Japan), as shown in Figure 5c. The LM bridge in the microchannel was stretched by the droplets on both sides under surface tension after external forces were removed, which acted in minimizing the surface area of liquid metal.[42] A pressure jump Δp on the concave meniscus is caused by the surface tension between LM and air, which is called Laplace pressure:[43]

$$\Delta p = \gamma_{ci}\left(\frac{1}{R_1} + \frac{1}{R_2}\right) = \gamma_{ci}\kappa \tag{1}$$

where R_1 and R_2 are the principal radii of curvature, γ_{ci} is the surface tension coefficient, and κ is twice the mean curvature. As shown in Figure 5b, the Laplace pressure points to the inside of

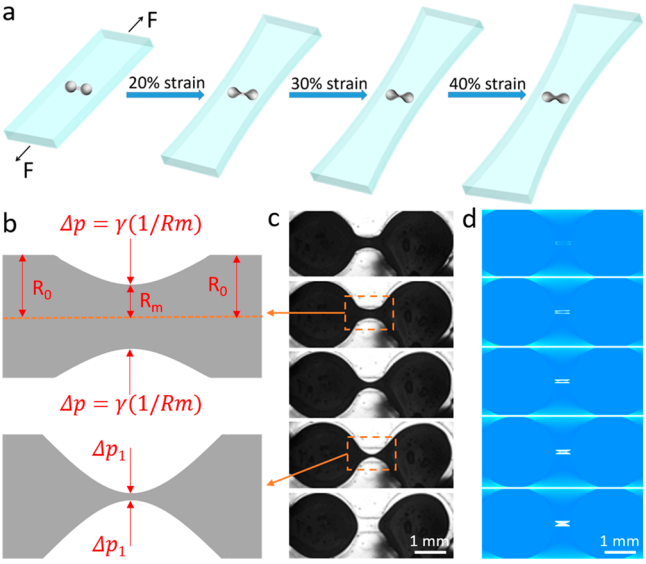

Figure 5. (a) Schematic diagram of the droplets contact process inside the H-LMDE composite. (b) Schematic diagram of pressure change during the contact and noncontact process between LMDs. (c) Image sequences of the formation and disconnection process of the LM bridge between the two LMDs in the microchannel. (d) Numerical simulation of the formation and disconnection process of the LM bridge in the microchannel.

the surface from outward. The largest pressure is built at the thinnest point with a minimum radius of R_{min} and can be expressed as

$$\Delta p = \gamma_{ci}\kappa = \gamma_{ci}\left(\frac{1}{R_{min}}\right) \tag{2}$$

As time t advanced, the bridge radius decreased under the action of pressure presented in eqs 1 and 2. The curvature and Laplace pressure built at the neck both increased at the same time, which were inversely proportional to the bridge radius. As a result, the LM was expelled with increasing velocity from the neck until the neck vanished. This is the spontaneous process of capillary breakup when the neck radius reaches a stability limit. The minimum necking radius of the LM bridge during capillary breakup follows a similar law:[44]

$$\frac{R_{min}}{R_0} = A\left[\sqrt{\frac{\sigma}{\rho R_0^3}}(t_p - t)\right]^{2/3} \tag{3}$$

where R_{min} represents the minimum radius of the LM bridge, R_0 represents the initial radius of the LM bridge, A is a constant, ρ is the material density, t_p denotes the bridge's breaking time, and t is the time interval before t_p. Obviously, the rupture speed of the capillary became faster as the surface tension coefficient increased. As a comparison, the COMSOL software was used to simulate the formation and disconnection process of the LM bridge in the microchannel, and the simulation results were well consistent with the experimental results (Figure 5d). In addition to the deformation caused by external forces, the changes in temperature and magnetic field could also make the LMDs interconnect and form conductive paths in the H-LMDE composites.

3.3. Thermal, Healable and Recyclable Properties of the H-LMDE Composites. Owing to the good thermal conductivity of liquid metal, the H-LMDE composites

https://doi.org/10.1021/acsami.1c23658
ACS Appl. Mater. Interfaces 2022, 14, 9597−9607

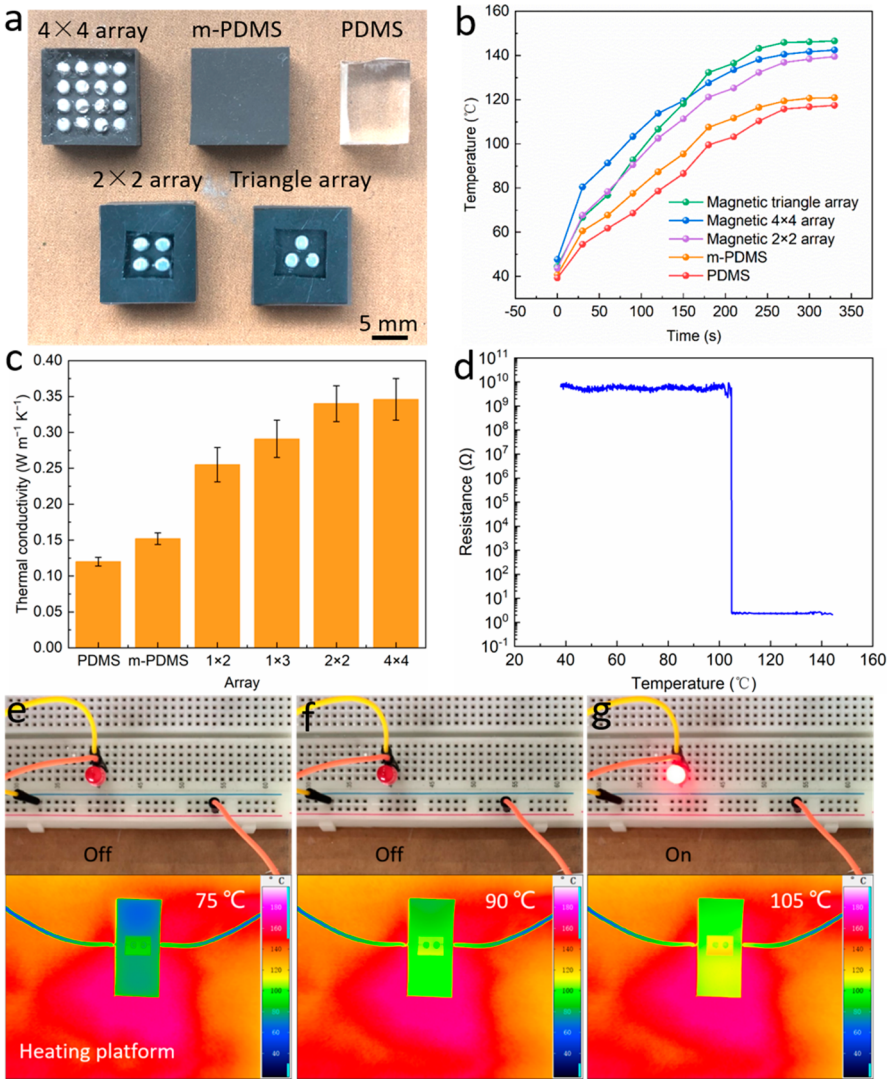

Figure 6. (a) Optical images of H-LMDE composites embedded with different numbers of LMDs and the PDMS samples. (b) Surface temperature change of PDMS samples and different types of H-LMDE composites. (c) Thermal conductivity of PDMS samples and different types of H-LMDE composites. (d) The resistance of two LMDs embedded H-LMDE composite at different temperatures. (e–g) Infrared images of two LMDs embedded H-LMDE composite used in a temperature alarm switch.

responded well to the changes in the surrounding thermal conditions. First of all, the H-LMDE composites (30 wt % CIP content) embedded with different numbers of droplets (Figure 6a) were prepared using different types of 3D-printed molds, and their thermal conductivities were compared with the pure PDMS matrix and the CIPs doped PDMS matrix (m-PDMS). The samples were put on a heating plate at 200 °C and an infrared camera was used to record the surface temperature in the center of the samples at different times (SI Figure S8). As shown in Figure 6b, the temperature of the samples embedded with LMDs raised faster than the PDMS samples. It was worth noting that the samples containing more droplets had the higher surface temperature due to the increase in liquid metal content. Different from the samples containing 4 × 4 and 2 × 2 droplet arrays, the droplets in the sample containing triangular droplet array were at the same distance from each other, which made the surface temperature of the sample slightly higher after 150 s. The composites with 30 wt % CIP content and different numbers of LMDs were selected as instances to perform the thermal conductivity measurement and the results were illustrated in Figure 6c. For comparison, the PDMS samples were also measured by the Hot Disk system. The thermal conductivity of pure PDMS was 0.121 $W \cdot m^{-1} \cdot K^{-1}$, which was close to that of magnetic PDMS. However, for the sample containing 4 × 4 droplet array, the value was 0.346 $W \cdot m^{-1} \cdot K^{-1}$, which was nearly three times than that of pure PDMS. After being embedded with liquid metal, the thermal conductivity of the composites had been significantly improved. The thermal conductivity of the composites gradually improved with the increase in the number of LMDs.

In addition, the relationship between the conductivity and the temperature of the H-LMDE composite was further explored. As shown in Figure 6d, when the temperature raised to about 105 °C, the resistance of the composite dropped sharply, changing from infinity to about 2.68 Ω. At high temperature, the deformation of the elastomer matrix caused the LMDs to connect with each other, forming a conductive path (SI Figure S9). According to this feature, the composite could be used as an ideal candidate for temperature alarm devices. To further illustrate the applicability of the composite, a temperature alarm system was developed by integrating the composite with a LED, Arduino breadboard and power module. A thermal infrared

https://doi.org/10.1021/acsami.1c23658
ACS Appl. Mater. Interfaces 2022, 14, 9597−9607

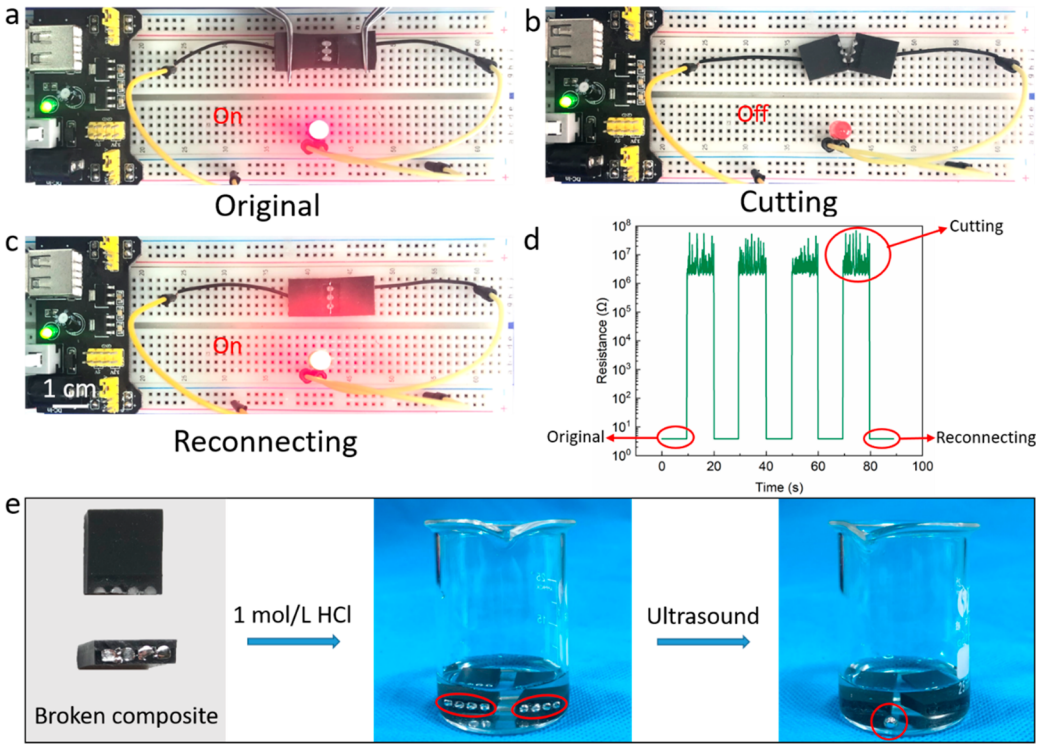

Figure 7. (a–c) Digital images of the three LMDs embedded H-LMDE composite integrated with breadboard and LED: cut and reconnection. Scale bar: 1 cm. (d) The corresponding resistance variation of three LMDs embedded H-LMDE composite. (e) The recycling process of the liquid metal in the four LMDs embedded H-LMDE composite.

camera was used to record the changes in the surface temperature of the composite, while observing the switching conditions of the LED (Figure 6e–g). When the temperature exceeded 105 °C, the LED was turned on and a temperature gradient appeared on the surface of the composite, which indicated that the composite deformed during the heating process (SI Movie S3). This phenomenon proved the good thermal conductivity of the H-LMDE composites and the feasibility of applying in temperature alarm devices.

Besides the satisfactory thermal conductivity, the H-LMDE composites delivered excellent healability, which was evaluated by conducting a fusion study of the composites interfaces. The Arduino breadboard, power module and a LED were employed to establish a constant voltage circuit to show the healability of the composite. The three LMDs embedded H-LMDE composite was severed with scissors and healed for several times under ambient conditions (Figure 7a–c). Since the initial resistance of the composite hardly changed (from 3.62 Ω to 3.59 Ω), constant LED luminance are observed after reconnection (Figure 7d). The good electrical performance was still obtained after healing the composite for several times, which was attributed to the good fluidity and electrical conductivity of the LMDs.[45]

Noteworthy, the feasibility and high efficiency of the recycling for the LMDs in the H-LMDE composites was also investigated in the experiment. It became easier and faster to recover the liquid metal from the damaged composites since the liquid metal was embedded in the elastomer matrix. As shown in Figure 7e, the damaged composite was first put into a beaker containing HCl solution (1 mol/L), the surface tension of the liquid metal immediately increased and it became easier to break away from the elastomer matrix. Then the mixed solution was stirred with a glass rod and treated with ultrasound in a KUDOS ultrasonic cleaner at a power of 50 W and frequency of 53 kHz under 25 °C to gradually separate the liquid metal from the elastomer matrix. The gathered minuscule LMDs merged in the presence of the acidic solution, as the acidic environment removed the oxide skin of liquid metal. Finally, a macroscopic and reusable LMD was obtained, which was capable to be manipulated or transferred readily. In this experiment, the recycling efficiency of the liquid metal was nearly 98% (SI Figure S10), which indicated the high reusability of liquid metal in the composites.

3.4. Application of the H-LMDE Composites. On the basis of good deformability and mechanically sensitive conductivity, the H-LMDE composites became an ideal candidate for flexible and wearable sensors. In order to further demonstrate the functionality of the composites, the two LMDs embedded H-LMDE composite was integrated on gloves to detect the finger motion. Besides, the H-LMDE composites containing 2 × 2 droplet array and 5 × 6 droplet array were developed for the detection of external magnetic field and compression. The PDMS with the CIP content of 30 wt % was selected as the matrix for the composites. Copper wires were embedded in the bottom of the composites to detect the resistance variation between the droplets. By integrating the H-LMDE composite on the gloves, the motion of finger could be recorded (Figure 8a,b). When bending the finger, the composite was synchronously stretched and the LMDs inside were deformed and interconnected accordingly. During this process, the resistance R dropped sharply and a conductive path was formed in the composite. Then the value of resistance recovered after the finger was outspread (Figure 8c).

When moving a permanent NdFeB magnet to the left side of the H-LMDE composite containing 2 × 2 droplet array (Figure 8d,e), the corresponding 2D intensity profile of resistance R was showed in Figure 8f. The left side of the droplet array was

https://doi.org/10.1021/acsami.1c23658
ACS Appl. Mater. Interfaces 2022, 14, 9597–9607

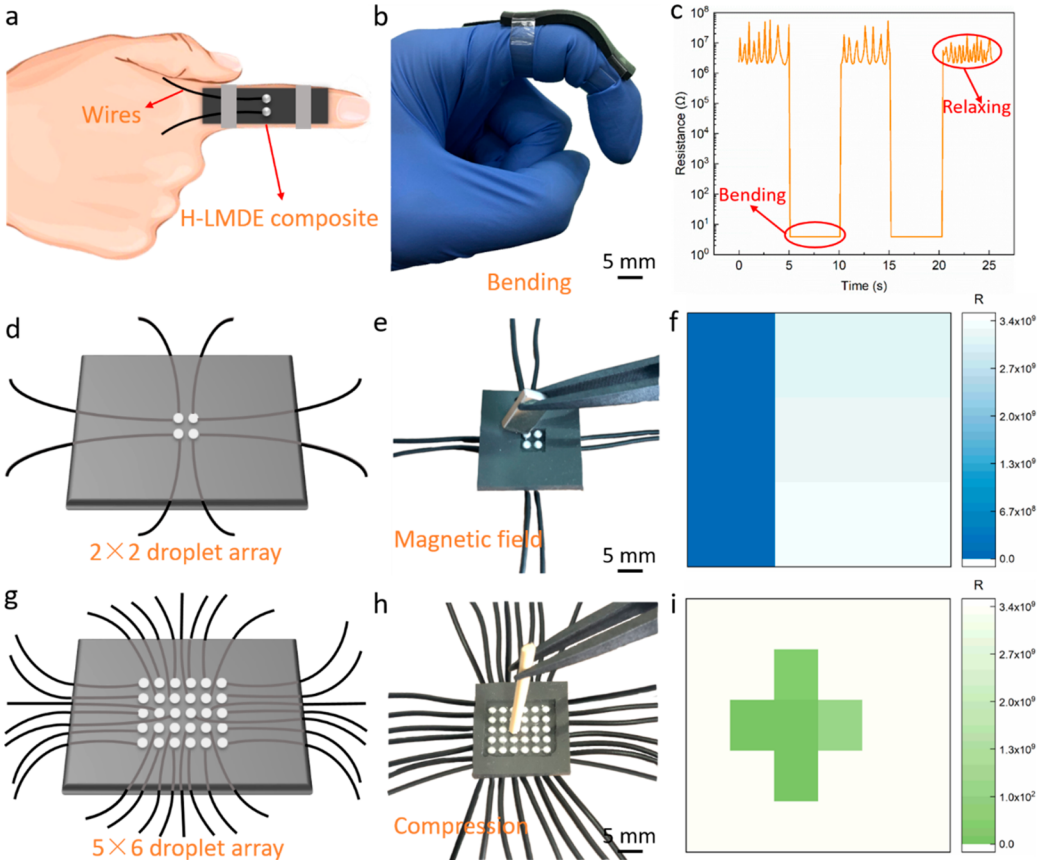

Figure 8. (a) Schematic diagram of the H-LMDE composites integrated on the finger. (b,c) Digital images of the H-LMDE composites integrated on gloves and the corresponding resistance variation when bending the finger. (d) Schematic diagram of the H-LMDE composite containing 2 × 2 droplet array. (e,f) Corresponding 2D intensity profile of *R* when moving a permanent NdFeB magnet to the left side of the 2 × 2 droplet array. (g) Schematic diagram of the H-LMDE composite containing 5 × 6 droplet array. (h,i) Corresponding 2D intensity profile of *R* when a part of the 5 × 6 droplet array was compressed.

deformed under the attracting of permanent magnet. The two LMDs on the left were interconnected in the microchannel due to the deformation of the array, which caused the decrease of resistance. The other parts of the array was less deformed, so the change in resistance was small, which also reflected the distribution of applied magnetic field (SI Figure S11). Moreover, the H-LMDE composites could be used to detect the pressure variation. A small wooden stick was used to press a certain part of the 5 × 6 droplet array (Figure 8g,h), causing the LMDs in the pressed part to connect with each other. Correspondingly, the resistance of the pressed part was reduced while the other parts remain unchanged. Figure 8i presented the corresponding 2D intensity profile of resistance *R*. As the pressure increased, the resistance of the pressed part decreased, showing the darker color than the unpressed parts. The mechanic-magnetic detection capability ensured the feasibility of the H-LMDE composites in future electronic devices.

4. CONCLUSION

In conclusion, a mechanically stable, conductivity reversible and recyclable H-LMDE composite has been developed. The composites could achieve mechanically sensitive conductivity through the formation and disconnection of the conductive path between the LMDs triggered by external forces, temperature, and magnetic fields. The mechanical and electrical properties of the composites were very stable during various mechanical deformations (stretching and bending). Moreover, the composites successfully realized the switching control of the LED circuit through the matrix's deformation. The thermal conductivity and fluidity of liquid metal endowed the composites with good heat transfer and healable properties. In addition, the LMDs embedded in the elastomer matrix could be recovered by immersing in HCl solution, which had a high recovery efficiency of 98%. Finally, different H-LMDE composites were used as sensors for mechano-magnetic detection. The excellent mechanical and electrical performance rendered the composites a promising material for flexible transient electronics, actuators, and robotics.

■ ASSOCIATED CONTENT

Supporting Information

The Supporting Information is available free of charge at https://pubs.acs.org/doi/10.1021/acsami.1c23658.

The switching of a LED through cyclic stretching process of the H-LMDE composite (Movie S1) (MP4)

The switching of a LED through cyclic bending process of the H-LMDE composite (Movie S2) (MP4)

The H-LMDE composite used in a temperature alarm switch (Movie S3) (MP4) (MP4)

The LMDE composites with vertical and horizontal arrangement of droplets (Figure S1); different kinds of 3D- printed molds and the H-LMDE composites with different arrangement of droplets (Figure S2); EDS mapping of the magnetic PDMS matrix of the H-LMDE

https://doi.org/10.1021/acsami.1c23658
ACS Appl. Mater. Interfaces 2022, 14, 9597−9607

composites (Figure S3); magnetic field strength versus to the distance away from the surface of N52 typed magnet (Figure S4); tensile strength and elastic modulus of the elastomer matrix with different CIP contents (Figure S5); resistance variation of the three and four LMDs embedded H-LMDE composite (Figure S6); test systems and resistance variation of the H-LMDE composite under cyclical magnetic field and compression (Figure S7); infrared images of the surface temperature for different samples over time (Figure S8); schematic diagram deformation of the H-LMDE composite during the heating process (Figure S9); recycling efficiency of the H-LMDE composites (30 wt % CIP content) with different numbers of LMDs (Figure S10); magnetic field distribution of the NdFeB magnet (Figure S11) (PDF)

AUTHOR INFORMATION

Corresponding Authors

Shouhu Xuan − *CAS Key Laboratory of Mechanical Behavior and Design of Materials, Department of Modern Mechanics, University of Science and Technology of China, Hefei 230027, China;* orcid.org/0000-0002-8232-9736; Email: xuansh@ustc.edu.cn

Xinglong Gong − *CAS Key Laboratory of Mechanical Behavior and Design of Materials, Department of Modern Mechanics, University of Science and Technology of China, Hefei 230027, China;* orcid.org/0000-0001-6997-9526; Email: gongxl@ustc.edu.cn

Authors

Xiaokang He − *CAS Key Laboratory of Mechanical Behavior and Design of Materials, Department of Modern Mechanics, University of Science and Technology of China, Hefei 230027, China*

Jianpeng Wu − *CAS Key Laboratory of Mechanical Behavior and Design of Materials, Department of Modern Mechanics, University of Science and Technology of China, Hefei 230027, China*

Shuaishuai Sun − *CAS Key Laboratory of Mechanical Behavior and Design of Materials, Department of Precision Machinery and Instrumentation, University of Science and Technology of China, Hefei, Anhui 230027, China*

Complete contact information is available at: https://pubs.acs.org/10.1021/acsami.1c23658

Notes

The authors declare no competing financial interest.

ACKNOWLEDGMENTS

Financial support from the National Natural Science Foundation of China (Grant Nos. 12072338 and 12132016), the Fundamental Research Funds for the Central Universities (WK2480000007, WK2480000009), and Joint Fund of USTC-National Synchrotron Radiation Laboratory (KY2090000055) are gratefully acknowledged. Thanks to the instrumentation support from engineering practice center of USTC.

ABBREVIATIONS

LM = liquid metal
LMDE = liquid metal droplets embedded elastomer
PDMS = polydimethylsiloxane
CIPs = carbonyl iron particles
HCl = Hydrochloric acid
T-LMDE = transparent liquid metal droplets embedded elastomer
M-LMDE = magnetic liquid metal droplets embedded elastomer
H-LMDE = hybrid liquid metal droplets embedded elastomer
DMA = dynamic mechanical analyzer
SEM = scanning electron microscopy
EDX = energy-dispersive X-ray spectrum
LED = light emitting diode

REFERENCES

(1) Bartlett, M. D.; Kazem, N.; Powell-Palm, M. J.; Huang, X. N.; Sun, W. H.; Malen, J. A.; Majidi, C. High Thermal Conductivity in Soft Elastomers with Elongated Liquid Metal Inclusions. *Proc. Nat. Acad. Sci. U.S.A.* **2017**, *114* (9), 2143−2148.

(2) Pan, C.; Liu, D.; Ford, M. J.; Majidi, C. Ultrastretchable, Wearable Triboelectric Nanogenerator Based on Sedimented Liquid Metal Elastomer Composite. *Adv. Mater. Technol.* **2020**, *5* (11), 202000754.

(3) Boley, J. W.; White, E. L.; Kramer, R. K. Mechanically Sintered Gallium-Indium Nanoparticles. *Adv. Mater.* **2015**, *27* (14), 2355−2360.

(4) Xu, J. Y.; Guo, H. D.; Ding, H. Y.; Wang, Q.; Tang, Z. Q.; Li, Z. J.; Sun, G. X. Printable and Recyclable Conductive Ink Based on a Liquid Metal with Excellent Surface Wettability for Flexible Electronics. *ACS Appl. Mater. Interfaces* **2021**, *13* (6), 7443−7452.

(5) Kazem, N.; Hellebrekers, T.; Majidi, C. Soft Multifunctional Composites and Emulsions with Liquid Metals. *Adv. Mater.* **2017**, *29* (27), 1605985.

(6) Kim, K. H.; Hong, S. K.; Jang, N. S.; Ha, S. H.; Lee, H. W.; Kim, J. M. Wearable Resistive Pressure Sensor Based on Highly Flexible Carbon Composite Conductors with Irregular Surface Morphology. *ACS Appl. Mater. Interfaces* **2017**, *9* (20), 17500−17508.

(7) Moriche, R.; Sanchez, M.; Jimenez, A.; Prolongo, S. G.; Urena, A. Strain Monitoring Mechanisms of Sensors Based on the Addition of Graphene Nanoplatelets into an Epoxy Matrix. *Compos. Sci. Technol.* **2016**, *123*, 65−70.

(8) Aziz, S.; Jung, K. C.; Chang, S. H. Stretchable Strain Sensor Based on a Nanocomposite of Zinc Stannate Nanocubes and Silver Nanowires. *Compos. Struct.* **2019**, *224*, 111005.

(9) Park, S. H.; Park, J.; Park, H. N.; Park, H. M.; Song, J. Y. Flexible Galvanic Skin Response Sensor Based on Vertically Aligned Silver Nanowires. *Sens. Actuators, B* **2018**, *273*, 804−808.

(10) Amjadi, M.; Pichitpajongkit, A.; Lee, S.; Ryu, S.; Park, I. Highly Stretchable and Sensitive Strain Sensor Based on Silver Nanowire-Elastomer Nanocomposite. *ACS Nano* **2014**, *8* (5), 5154−5163.

(11) Tavakoli, M.; Malakooti, M. H.; Paisana, H.; Ohm, Y.; Marques, D. G.; Lopes, P. A.; Piedade, A. P.; de Almeida, A. T.; Majidi, C. EGaIn-Assisted Room-Temperature Sintering of Silver Nanoparticles for Stretchable, Inkjet-Printed, Thin-Film Electronics. *Adv. Mater.* **2018**, *30* (29), 1801852.

(12) Liao, X.; Zhang, Z.; Liang, Q.; Liao, Q.; Zheng, Y. Flexible, Cuttable, and Self-Waterproof Bending Strain Sensors Using Micro-cracked Gold Nanofilms@Paper Substrate. *ACS Appl. Mater. Interfaces* **2017**, *9* (4), 4151−4158.

(13) Song, Y. X.; Xu, W. M.; Rong, M. Z.; Zhang, M. Q. A Sunlight Self-Healable Transparent Strain Sensor with High Sensitivity and Durability Based on a Silver Nanowire/Polyurethane Composite Film. *J. Mater. Chem. A* **2019**, *7* (5), 2315−2325.

(14) Buettel, G.; Joppich, J.; Hartmann, U. Micromachined Ssilicon Cantilevers with Integrated High-Frequency Magnetoimpedance Ssensors for Simultaneous Strain and Magnetic Field Detection. *Appl. Phys. Lett.* **2017**, *111* (23), 232401.

(15) Yun, J.; Song, C.; Lee, H.; Park, H.; Jeong, Y. R.; Kim, J. W.; Jin, S. W.; Oh, S. Y.; Sun, L.; Zi, G.; Ha, J. S. Stretchable Array of High-Performance Micro-Supercapacitors Charged with Solar Cells for Wireless Powering of an Integrated Strain Sensor. *Nano Energy* **2018**, *49*, 644−654.

(16) Dou, Y.; Luo, J.; Qi, L.; Lian, H.; Huang, J. Drop-on-Demand Printing of Recyclable Circuits by Partially Embedding Molten Metal Droplets in Plastic Substrates. *J. Mater. Process. Technol.* **2021**, *297*, 117268.
(17) Kim, S.; Oh, J.; Jeong, D.; Bae, J. Direct Wiring of Eutectic Gallium-Indium to a Metal Electrode for Soft Sensor Systems. *ACS Appl. Mater. Interfaces* **2019**, *11* (22), 20557−20565.
(18) Chen, Y.; Liu, Z.; Zhu, D.; Handschuh-Wang, S.; Liang, S.; Yang, J.; Kong, T.; Zhou, X.; Liu, Y.; Zhou, X. Liquid Metal Droplets with High Elasticity, Mobility and Mechanical Robustness. *Mater. Horiz.* **2017**, *4* (4), 591−597.
(19) Jin, S. W.; Jeong, Y. R.; Park, H.; Keum, K.; Lee, G.; Lee, Y. H.; Lee, H.; Kim, M. S.; Ha, J. S. A Flexible Loudspeaker Using the Movement of Liquid Metal Induced by Electrochemically Controlled Interfacial Tension. *Small* **2019**, *15* (51), 1905263.
(20) Andrews, J. B.; Mondal, K.; Neumann, T. V.; Cardenas, J. A.; Wang, J.; Parekh, D. P.; Lin, Y.; Ballentine, P.; Dickey, M. D.; Franklin, A. D. Patterned Liquid Metal Contacts for Printed Carbon Nanotube Transistors. *ACS Nano* **2018**, *12* (6), 5482−5488.
(21) Chen, Y. L.; Nguyen, Y.; Wu, S. E.; Chun, Y. C.; Chuang, C.; Hsieh, Y. P.; Hofmann, M. Patterned Liquid Metal Contacts for High Density, Stick-and-Peel 2D Material Device Arrays. *Nanoscale* **2018**, *10* (30), 14510−14515.
(22) Park, C. W.; Moon, Y. G.; Seong, H.; Jung, S. W.; Oh, J. Y.; Na, B. S.; Park, N. M.; Lee, S. S.; Im, S. G.; Koo, J. B. Photolithography-Based Patterning of Liquid Metal Interconnects for Monolithically Integrated Stretchable Circuits. *ACS Appl. Mater. Interfaces* **2016**, *8* (24), 15459−15465.
(23) Chen, G.; Deng, X.; Zhu, L.; Handschuh-Wang, S.; Gan, T.; Wang, B.; Wu, Q.; Fang, H.; Ren, N.; Zhou, X. Recyclable, Weldable, Mechanically Durable, and Programmable Lliquid Metal-Elastomer Composites. *J. Mater. Chem. A* **2021**, *9* (17), 10953−10965.
(24) Teng, L.; Ye, S.; Handschuh-Wang, S.; Zhou, X.; Gan, T.; Zhou, X. Liquid Metal-Based Transient Circuits for Flexible and Recyclable Electronics. *Adv. Funct. Mater.* **2019**, *29* (11), 1808739.
(25) Markvicka, E. J.; Bartlett, M. D.; Huang, X.; Majidi, C. An Autonomously Electrically Self-Healing Liquid Metal-Elastomer Composite for Robust Soft-Matter Robotics and Electronics. *Nat. Mater.* **2018**, *17* (7), 618−624.
(26) Liu, H.; Xin, Y.; Lou, Y.; Peng, Y.; Wei, L.; Zhang, J. Liquid Metal Gradient Fibers with Reversible Thermal Programmability. *Mater. Horiz.* **2020**, *7* (8), 2141−2149.
(27) Haque, A. B. M. T.; Tutika, R.; Byrum, R. L.; Bartlett, M. D. Programmable Liquid Metal Microstructures for Multifunctional Soft Thermal Composites. *Adv. Funct. Mater.* **2020**, *30* (25), 2000832.
(28) Dehnavi, F. N.; Safdari, M.; Abrinia, K.; Sheidaei, A.; Baniassadi, M. Numerical Study of the Conductive Liquid Metal Elastomeric Composites. *Mater. Today Commun.* **2020**, *23*, 100878.
(29) Daalkhaijav, U.; Yirmibesoglu, O. D.; Walker, S.; Menguc, Y. Rheological Modification of Liquid Metal for Additive Manufacturing of Stretchable Electronics. *Adv. Mater. Technol.* **2018**, *3* (4), 1700351.
(30) Ou, M.; Qiu, W.; Huang, K.; Feng, H.; Chu, S. Ultrastretchable Liquid Metal Electrical Conductors Built-in Cloth Fiber Networks for Wearable Electronics. *ACS Appl. Mater. Interfaces* **2020**, *12* (6), 7673−7678.
(31) Zhang, Q.; Roach, D. J.; Geng, L.; Chen, H.; Qi, H. J.; Fang, D. Highly Stretchable and Conductive Fibers Enabled by Liquid Metal Dip-Coating. *Smart Mater. Struct.* **2018**, *27* (3), No. 035019.
(32) Wang, D.; Liu, D.; Xu, J.; Fu, J.; Wu, K. Highly Thermoconductive yet Ultraflexible Polymer Composites with Superior Mechanical Properties and Autonomous Self-Healing Functionality via a Binary Filler Strategy. *Mater. Horiz.* **2022**, DOI: 10.1039/D1MH01746B.
(33) Tutika, R.; Haque, A. B. M. T.; Bartlett, M. D. Self-Healing Liquid Metal Composite for Reconfigurable and Recyclable Soft Electronics. *Commun. Mater.* **2021**, *2* (1), 64.
(34) Krisnadi, F.; Nguyen, L. L.; Ankit; Ma, J.; Kulkarni, M. R.; Mathews, N.; Dickey, M. D. Directed Assembly of Liquid Metal-Elastomer Conductors for Stretchable and Self-Healing Electronics. *Adv. Mater.* **2020**, *32*, 2001642.
(35) Li, F.; Qin, Q.; Zhou, Y.; Wu, Y.; Xue, W.; Gao, S.; Shang, J.; Liu, Y.; Li, R. W. Recyclable Liquid Metal-Based Circuit on Paper. *Adv. Mater. Technol.* **2018**, *3* (8), 1800131.
(36) Mao, Y.; Wu, Y.; Zhang, P.; Yu, Y.; He, Z.; Wang, Q. Nanocellulose-Based Reusable Liquid Metal Printed Electronics Fabricated by Evaporation-Induced Transfer Printing. *J. Mater. Sci. Technol.* **2021**, *61*, 132−137.
(37) Chen, Y.; Zhou, T.; Li, Y.; Zhu, L.; Handschuh-Wang, S.; Zhu, D.; Zhou, X.; Liu, Z.; Gan, T.; Zhou, X. Robust Fabrication of Nonstick, Noncorrosive, Conductive Graphene-Coated Liquid Metal Droplets for Droplet-Based, Floating Electrodes. *Adv. Funct. Mater.* **2018**, *28* (8), 1706277.
(38) Mineart, K. P.; Lin, Y.; Desai, S. C.; Krishnan, A. S.; Spontak, R. J.; Dickey, M. D. Ultrastretchable, Cyclable and Recyclable 1- and 2-Dimensional Conductors Based on Physically Cross-Linked Thermoplastic Elastomer Gels. *Soft Matter* **2013**, *9* (32), 7695−7700.
(39) Hu, L.; Wang, H.; Wang, X.; Liu, X.; Guo, J.; Liu, J. Magnetic Liquid Metals Manipulated in the Three-Dimensional Free Space. *ACS Appl. Mater. Interfaces* **2019**, *11* (8), 8685−8692.
(40) Pan, C.; Markvicka, E. J.; Malakooti, M. H.; Yan, J.; Hu, L.; Matyjaszewski, K.; Majidi, C. A Liquid-Metal-Elastomer Nanocomposite for Stretchable Dielectric Materials. *Adv. Mater.* **2019**, *31* (23), 1900663.
(41) Cantournet, S.; Desmorat, R.; Besson, J. Mullins Effect and Cyclic Stress Softening of Filled Elastomers by Internal Sliding and Friction Thermodynamics Model. *Int. J. Solids Struct.* **2009**, *46* (11−12), 2255−2264.
(42) Eggers, J.; Villermaux, E. Physics of Liquid Jets. *Rep. Prog. Phys.* **2008**, *71* (3), No. 036601.
(43) Mugele, F.; Baret, J. C. Electrowetting: From Basics to Applications. *J. Phys.: Condens. Matter* **2005**, *17* (28), R705−R774.
(44) Zhu, X.; Yang, F.; Zhao, S.; Wang, H.; Niu, C.; Rong, M. Liquid-Metal Capillary Switch for Electrical Power Application. *Appl. Phys. Lett.* **2020**, *117* (26), 263701.
(45) Zhang, M. K.; Yao, S. Y.; Rao, W.; Liu, J. Transformable Soft Liquid Metal Micro/Nanomaterials. *Mater. Sci. Eng. R-Rep.* **2019**, *138*, 1−35.